

Optimizing the electroforming process for full-shell X-ray optics

Panini Singam^{a,*}, Chet Speegle^b, Amy Meekham^c, Jeffery Kolodziejczak^b, David Banks^c, Wayne Baumgartner^b, Jessica Gaskin^b, Stephen Bongiorno^b, Brian Ramsey^b, David D Smith^b, Danielle Gurgew^a, and Nicholas Thomas^b

^aUniversities Space Research Association, Science and Technology Institute/NASA MSFC, Huntsville, Alabama, United States

^bNASA Marshall Space Flight Center, Huntsville, Alabama, United States

^cJacobs Engineering Group Inc., Tullahoma, Tennessee, United States

ABSTRACT. Electroforming replication technology at the Marshall Space Flight Center has a long heritage of producing high-quality, full-shell X-ray mirrors for various applications. Nickel alloys are electroformed onto a super-polished mandrel in the electroforming process and then separated to form the replicated full-shell optic. Various parameters in the electroplating configuration could result in the non-uniformity of the shell's thickness. Thickness non-uniformities primarily occur due to the non-uniform electric field distribution in the electroforming tank during deposition. Using COMSOL Multiphysics simulations, we studied the electric field distributions during the deposition process. Using these studies, we optimized the electric field distribution and strength inside the tank using customized shields and insulating gaskets on the mandrel. These efforts reduced the thickness non-uniformity from over 20% to under 5%. Improving the thickness uniformity of the shell aids in better mounting and aligning shells in the optics module. Optimization of the electroforming process, in some cases, improved the optical performance of the shells. Using finite element modeling, we estimated the effect of electroforming stress on the figure errors of the replicated optics. We observed that the electroforming stress predominantly affects the figure toward the ends of the optics. We presented COMSOL optimization of the electroforming process and the experimental results validating these simulations. We also discuss modeling experimental results of the replication figure errors due to electroforming stresses.

© The Authors. Published by SPIE under a Creative Commons Attribution 4.0 International License. Distribution or reproduction of this work in whole or in part requires full attribution of the original publication, including its DOI. [DOI: [10.1117/1.JATIS.10.3.034001](https://doi.org/10.1117/1.JATIS.10.3.034001)]

Keywords: X-ray optics; electroforming; astrophysics; high-resolution imaging; COMSOL simulations; thin film stress

Paper 24026G received Mar. 21, 2024; revised Jun. 18, 2024; accepted Jun. 24, 2024; published Jul. 16, 2024.

1 Introduction

Electroformed replication technology is a proven technique for fabricating astronomical X-ray optics. The ability to produce full-shell, lightweight, and consistent high-resolution optics has made this technology attractive for developing high-throughput astronomical X-ray telescopes. The National Aeronautics and Space Administration (NASA) Marshall Space Flight Center (MSFC) has three decades of experience developing grazing incidence X-ray optics through electroformed replication.¹⁻³ In this approach, electroless-Nickel-coated aluminum mandrels are figured and super-polished to match the desired optics prescription and the required surface

*Address all correspondence to Panini Singam, srikanthpanini.singam@nasa.gov

roughness. After placing a mandrel in the electroforming tank and growing the desired thickness Nickel alloy shell, the shell is carefully separated by cooling the mandrel. We currently use a nickel–cobalt (NiCo) alloy for electroforming due to its high tensile strength and Young’s modulus. The inner surface of the replicated NiCo shell is a replica of the polished mandrel surface profile and roughness. A single mandrel can be reused to replicate multiple shells without significantly degrading the surface quality, making it a cost-effective technique for producing multiple mirror shells.

As the total external reflection of X-rays is limited to small graze angles (typically $<1^\circ$), the effective geometric area of the optic is scaled down by a factor of the sine of the graze angle. To increase the effective area, multiple confocal shells with different diameters and graze angles are arranged concentric to one another. The thickness of each shell can limit this arrangement. The electroforming replication process produces thin, full shells that are relatively straightforward to align and mount. Once the mandrels are polished, replication is relatively inexpensive, making multiple identical mirror modules on a single observatory beneficial. BeppoSAX,⁴ X-ray Multi-Mirror Mission (XMM)-Newton,⁵ Swift X-ray telescope,⁶ eROSITA,⁷ Astronomical Roentgen Telescope X-ray Concentrator (ART-XC),⁸ and Imaging X-ray Polarimetry Explorer (IXPE)⁹ are a few examples of this. Pioneering replication technology over the last couple of decades, MSFC has produced X-ray optics for balloon flights [high energy replicated optics (HERO)^{10,11}], sounding rocket flights [Focusing Optics X-ray Solar Imager (FOXSI)-I,¹² FOXSI-II,¹³ FOXSI-III,¹⁴ and FOXSI-IV¹⁵], and orbiting satellites (ART-XC,¹⁶ IXPE⁹). Replication technology has also made high-resolution X-ray imaging optics for the National Ignition Facility¹⁷ and neutron imaging optics for the National Institute of Standards and Technology.

Although replication produces mirrors about two orders of magnitude thinner than those used for the Chandra mirrors,¹⁸ they have yet to achieve sub-arcsecond angular resolution. Residual profile errors from mandrel polishing, electroforming stresses, shell separation stresses, and mounting errors contribute to performance degradation. We continue to investigate improving these processes at various stages of fabrication to meet the angular resolution requirement for the Lynx mission concept¹⁹ and for other future astrophysics missions.

Ensuring shell thickness uniformity is vital for producing high-quality optics and optimally aligning and mounting shells into mirror module assemblies. Uniform shell thickness, especially at the edges, directly helps the alignment and mounting of the shell to the optics assembly. As shown in Figs. 4 and 8 in the paper, non-optimized gaskets result in significantly thicker edges than the rest of the shell. As the ends of optics are bonded to the assembly structure using epoxy, the non-uniformity in thickness results in bond line thickness errors that affect the bond’s strength and stiffness and change the structure’s dynamic response. Hence, having a uniform shell thickness benefits the performance of a flight mirror module assembly. Optimization of the electroforming process, in some cases, even improves the optical performance of the shells (see Sec. 5.5).¹⁷ We note that X-ray mirrors for the XMM-Newton telescope reported $\sim 20\%$ variation in axial thickness (Ref. 20), with the edges of the shell are significantly thicker than the nominal value. Ito et al.²¹ conducted a simulation-based study to regulate the thickness non-uniformity near the edges of the shell using optimized shields and cathode position. Using COMSOL simulations and experimental diagnostic tools, we study and optimize the electric field distribution present during mirror shell electro-deposition. Some of these results are presented in an *International Society for Optics and Photonics* proceeding.²² We also used COMSOL simulations to study the effect of electroforming stress on the optics’ replication figure errors. An overview of the electroforming process is described in Sec. 2, and COMSOL simulations to optimize the thickness variations and experimental validations are presented in Secs. 3 and 4, respectively. Section 5 presents the finite element modeling (FEM) to estimate the effects of the electroforming stress on the replication errors.

2 NiCo Electroforming Replication Process

In the electroforming process, the material from the anodes is electrodeposited onto the mandrel, which acts as a cathode. Unlike traditional electroplating, the mandrel surface is passivated with an oxide layer to reduce the adhesion of the plated material. We use nickel (Ni) and cobalt (Co)

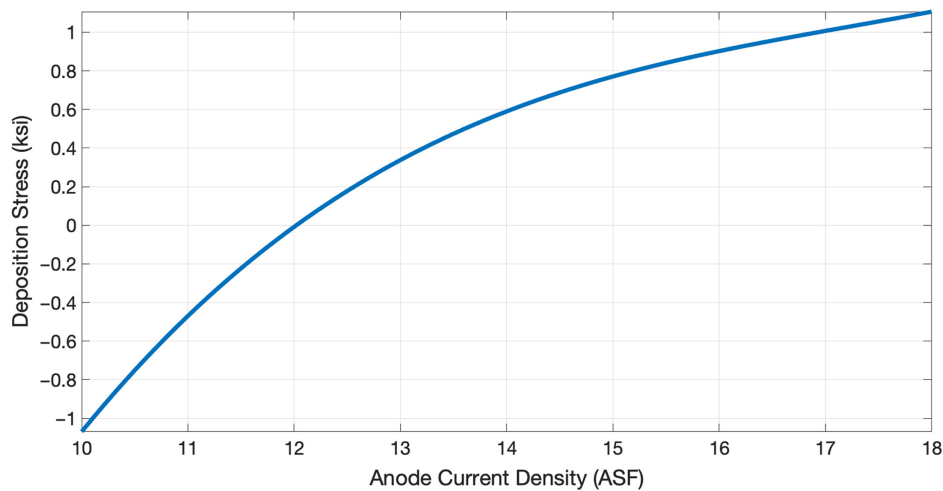


Fig. 1 Deposition stress versus the applied current density of the electroforming tank. Positive deposition stress indicates tensile stress, and negative stress represents compressive stress.

anodes to deposit the NiCo alloy on the mandrel. Pure nickel is a very ductile material showing signs of yielding at low applied stresses. We have observed that the yield strength of NiCo with an 85% to 15% ratio of Ni to Co is much higher and produces stable shells.² We use NiCo sulfamate as an electrolyte with properties that are regulated to have an optimal deposition stress for electroplating. Adhesion control and deposition stress control are vital for successful electroforming. Low adhesion and compressive deposition stress can lead to the premature release of the shell during electroforming with the risk of damaging the mandrel. Conversely, high adhesion and large tensile deposition stress deform the shell, making it difficult to release from the mandrel.²³ Deposition stresses are controlled by regulating the electrolyte temperature and additive salts to the nickel sulfamate electrolyte. Deposition rates, controlled by the anode current density, are vital in controlling deposition stresses. Figure 1 shows an example of the measured stress as a function of the current density in the electroforming tank.

The deposited shell thickness growth per unit of time is directly proportional to the local current density on the mandrel surface. The electric field distribution inside the tank depends on the electroforming tank geometry and mandrel dimensions. In the electroforming tank, several anodes of nickel and cobalt are placed symmetrically around the mandrel to ensure azimuthal field uniformity and, hence, the shell's thickness. The mandrel in the center rotates around its axis throughout the deposition to further improve the thickness uniformity. However, due to finite dimensions and the axial slope of the mandrel, the thickness of the shell varies axially. Thickness non-uniformity is more prominent near the shell's ends due to the mandrel surface's abrupt discontinuity. Insulating gaskets and shields regulate the local current densities at the mandrel surface to maintain the uniformity of the axial thickness of the shell. Figure 2 shows the schematic of the electroforming setup with anodes, mandrels, gaskets, and shields.

Our mandrels consist of parabolic and hyperbolic profiles polished onto a monolithic electroless-NiP-coated aluminum cylinder. Precise polishing at the ends of the mandrels is challenging due to the finite size of the polishing tools. Hence, the axial length of the mandrel on both the parabolic and hyperbolic sides is slightly larger than the intended optic dimensions. This end-cap region on either side of the mandrel, which does not form a part of the optic, helps obtain good quality end regions during polishing. End-cap regions are separated from the optic segment of the mandrels by a small groove (single-piece mandrel) or a detachable block (three-piece mandrel). During the electroforming process, insulating gaskets are used at the boundaries of the optic and end-cap region of the mandrel to restrict plating. Insulating shields are used at both ends of the mandrel to control the local electric field. Thus, gaskets and shields are primarily used to define the boundaries of the shell. However, their dimensions can be optimized to regulate the local electric field distribution for uniform thickness deposition.

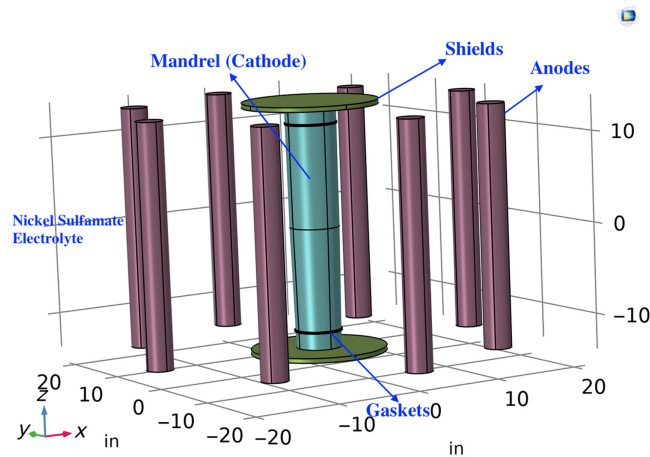


Fig. 2 Schematic of the electroforming tank.

3 COMSOL Simulations to Optimize the Electroforming Process

We use the COMSOL Multiphysics[®] software package²⁴ to model the electric field distribution inside the plating tank for a given geometry and mandrel. COMSOL allows the exact tank geometry specifications to be input to calculate the field distribution. The electric field distribution across the mandrel gives a corresponding deposition thickness distribution. Depending on the size and shape of the mandrels, the electric field varies axially, resulting in a non-uniform thickness distribution. Using these simulations, we design optimal dimensions of gaskets and shields to control the field distribution. As a result, we observed a significant improvement in the thickness uniformity of the shells.

3.1 Thickness Uniformity at the Mirror Shell Boundaries

The electroformed mandrel experiences higher electric fields near the gaskets, resulting in a greater thickness near the edge of the optics. Thickness uniformity can be improved by increasing the radial height of the gasket (GH) above the surface of the mandrel. We considered a cylindrical mandrel of 16 cm diameter and 30 cm axial length for simulations. Gaskets are placed at 5 cm from the ends on both ends. For a small GH (defined by the distance from the surface of the mandrel to the outer diameter of the gasket) of 5 mm, the mirror shell edges are $\sim 19\%$ thicker than in the mid-region of the mirror shell. Figure 3 shows the variation in thickness distribution near the shell edges for different GHs. The thickness distribution of a cylindrical mirror shell using a gasket with a 5-mm height is shown in Fig. 3(a). The edges of this shell are significantly thicker than the rest of the optic. The thickness distribution resulting from using a larger diameter gasket with a gasket height of 4 cm, shown in Fig. 3(b), indicates a more uniform shell thickness. Figure 4 shows the axial shell thickness simulation results for various gasket heights. The

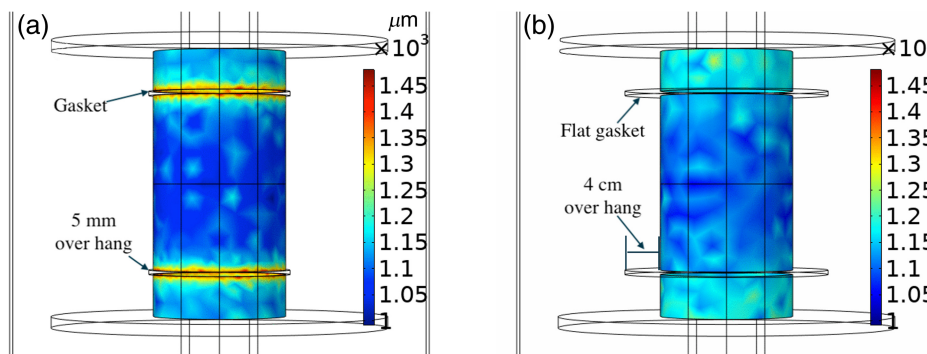


Fig. 3 Thickness distribution of mirror shells for gaskets with different heights. (a) A cylindrical mandrel with GH = 5 mm. (b) A cylindrical mandrel with GH = 4 cm.

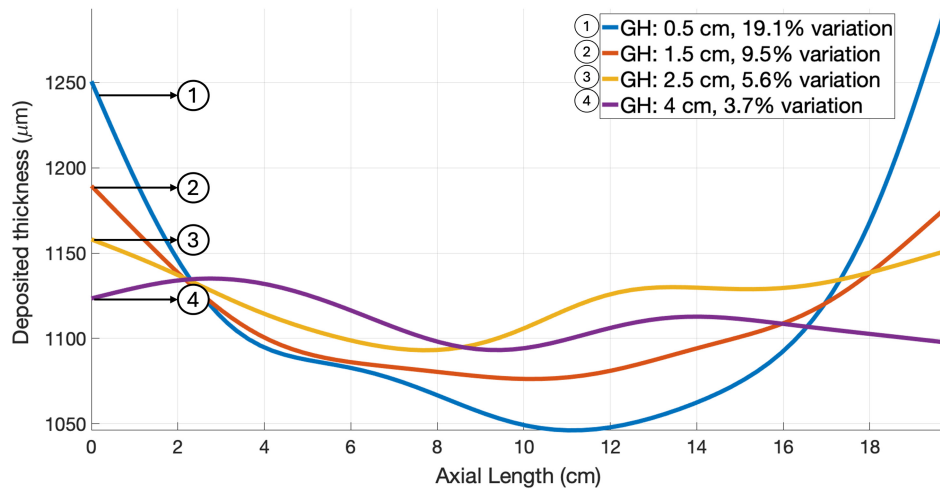


Fig. 4 Axial shell thickness simulation results for various gasket heights. The label indicates gasket heights and the corresponding percentage of peak-to-valley thickness variation.

thickness uniformity at the edges systematically improves as the GH is increased. Increasing the GH to 4 cm from 5 mm can reduce the axial thickness variation to 3.7% from 19%.

3.2 Gasket Optimization for Large Graze Angle Optics

As the grazing angle of the optics changes, the relative anode-mandrel distance and slope change across the axial length. This results in a gradient in the axial thickness of the shell. This effect is more pronounced for the optics with large graze angles. The diameters of the mandrel's top and bottom ends are significantly different for large graze angles. Figure 5 shows the axial thickness variation for three mandrel geometries with varied graze angles. We considered a GH of 4 cm for this simulation to minimize the edge thickness variation. The axial thickness variation increases with the grazing angle of the mandrel. Unlike small height gaskets, the thickness variation trend is distributed across the axial length of the mandrel. The larger diameter end of the mandrel experiences a higher deposition rate. For a cylindrical mandrel, the axial thickness variation with large gaskets is $\sim 3.7\%$ and looks much flatter across the axial length of the optic. This value significantly increases to 12.3% for a mandrel with a 3-deg graze angle.

The thickness uniformity of the shell with large grazing angles can be improved using different gasket dimensions for each end of the mandrel. For example, the 3-deg graze angle mandrel experiences relatively smaller electric fields on the smaller end of the optic. Optimally reducing the GH on the smaller end increases the electric field to negate this effect. Fixing the GH on the

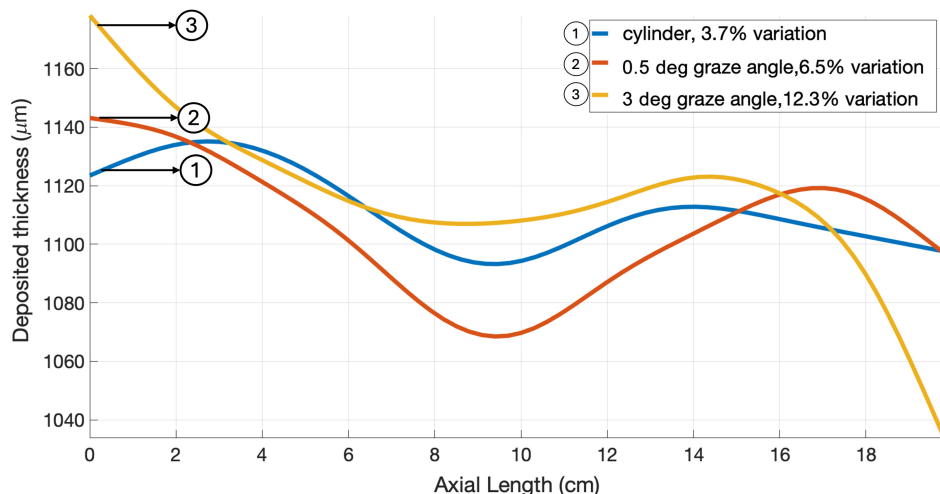


Fig. 5 Axial thickness variation for three different mandrels with different graze angles.

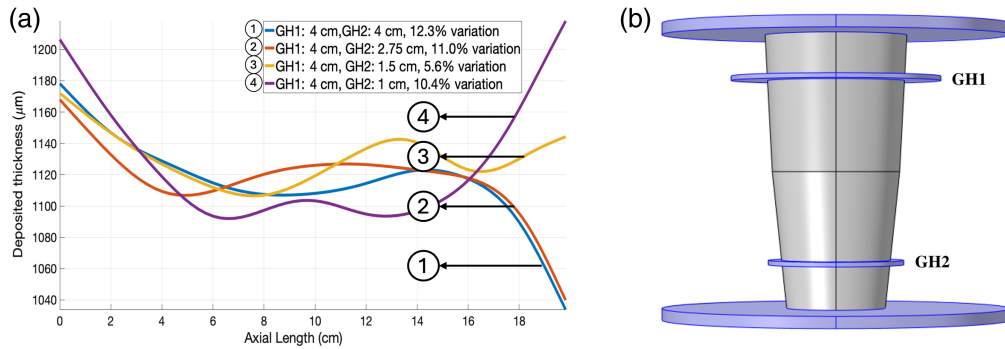


Fig. 6 Effect of GH optimization on the axial thickness distribution of the mirror shell. (a) Axial thickness distribution for a mandrel with a 3-deg graze angle for various gasket configurations. GH1 and GH2 are gasket heights on large and small ends, respectively. (b) The schematic of the optimal gasket configuration for a mandrel with a large graze angle. Using different gasket dimensions on each end improves the thickness uniformity.

larger end and gradually reducing the GH on the smaller end yields a more uniform thickness distribution. However, if the GH is reduced to below the optimal value, the field increases, resulting in much thicker ends. Figure 6(a) shows the axial thickness distribution for a mandrel with a 3-deg graze angle for various gasket configurations. The gasket height on the larger end (GH1) is fixed at 4 cm in all cases, whereas the gasket height on the smaller end (GH2) of the optic is varied for different cases. The optimal configuration with a GH2 of 1.5 cm yields $\sim 5.6\%$ thickness variation measured from peak to valley. However, further reducing the GH2 to 1 cm above the surface increases the thickness at the smaller end beyond the desired value, resulting in a 10.4% variation. Figure 6(b) shows the schematic of the optimal gasket configuration for a mandrel with a large graze angle.

3.3 Gaskets for Single-Piece Mandrels

Gaskets with large heights, called flat gaskets, are often used with three-piece mandrels. In a three-piece mandrel, the end caps can be detached from the optics-plating portion with the help of screws. Hence, inserting a large flat gasket between the three different parts of the mandrel is easy. However, for a single-piece mandrel, the end caps are part of the primary structure and are separated from the shell-forming region of the mandrel by a machined groove in which the gasket sits. Currently, the groove depth limits the maximum usable GH to 5 mm, resulting in thickness non-uniformity at the edges of the replicated mirror shell.

To maintain the thickness uniformity near the edges of gaskets with smaller GHs, we place a copper strip around the circumference of the gasket to act as a cathode region. This arrangement redirects the excess electric field from the edges of the forming optics to the gasket. The copper strip on the gasket gets electroplated, making the optic edges more uniform in thickness. Figure 7 shows the effect of the copper strip on the thickness uniformity of the single-piece mandrel.

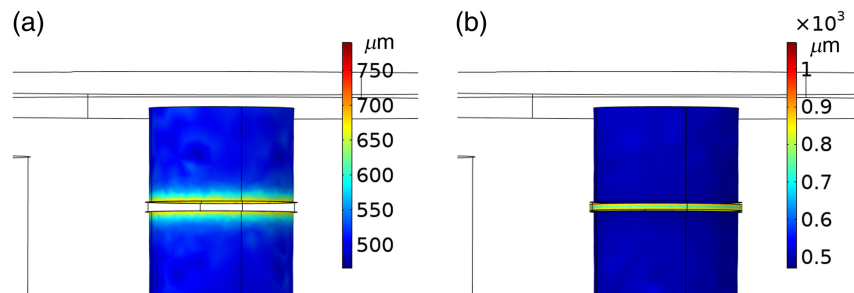


Fig. 7 Effect of the gasket copper strip on the shell thickness uniformity of the single-piece mandrel. The values in the color bar are in micrometers. (a) Without the copper strip. The optics portion experiences large thickness variation near the end caps. (b) With the copper strip. The copper strip gets electroplated, leaving the optics portion with uniform edges.

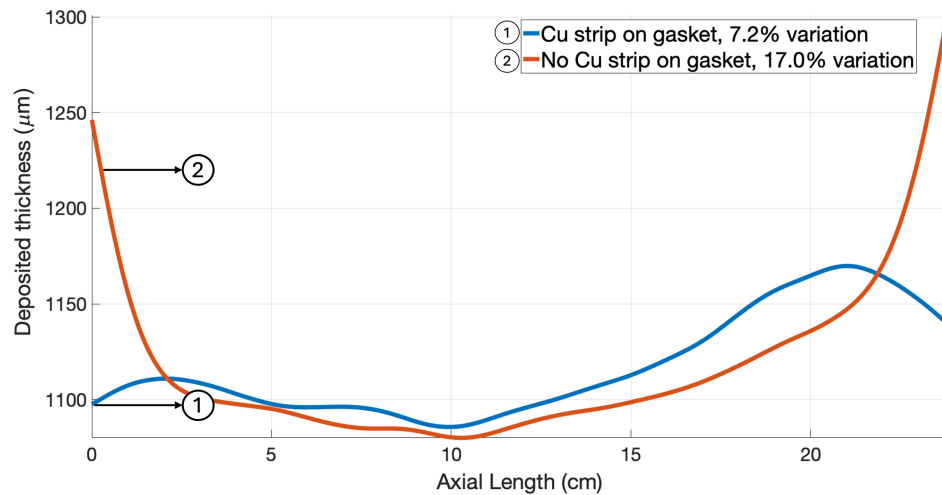


Fig. 8 Axial thickness variation of the optics with and without the copper strip on the gasket. Using a copper strip, the thickness uniformity improved to 7% from 17%.

Figure 7(a) shows the deposited shell thickness near the gasket without a copper strip. The optics portion experiences considerable thickness non-uniformity close to the end caps. Figure 7(b) shows the thickness distribution with a copper strip on the gasket. The copper strip gets electroplated, leaving the optics portion with uniform edges. Figure 8 shows the axial thickness variation of the optics with and without the copper strip on the gasket. Using a copper strip, the thickness uniformity improved to 7% from 17% without the strip.

3.4 Optimizing Shield Dimensions for Large Mandrels

Large-diameter gaskets with different GHs on both ends regulate the electric field distribution across the axial surface of the mandrel. However, gaskets of a few centimeters in height cannot influence the total electric field across the surface of a large mandrel. For mandrels with axial lengths larger than 30 cm, the influence of the gaskets is localized close to the ends. Using extremely large-diameter gaskets of several 10 s of centimeters in diameter is impractical. Hence, we optimize the shield dimensions to regulate the overall electric fields of large mandrels. Even though shields are generally placed at the ends of the mandrel after the end caps, the large shield diameters can influence the field distribution along the mandrel. As the slope of the optics makes one end of the mandrel larger than the other, we use different shield diameters on each end to counter the effect. Figure 9 shows the shell thickness variation of a mandrel with an axial

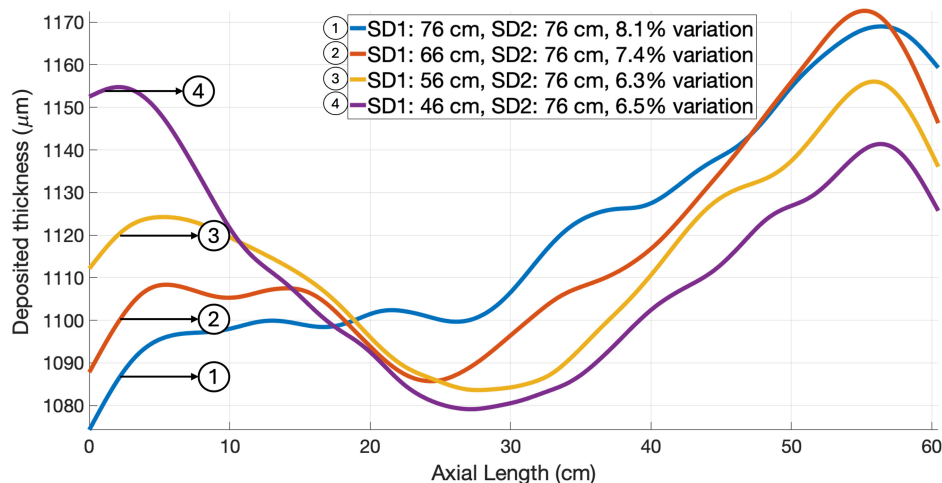


Fig. 9 Axial thickness variation of a mandrel with an axial length of 60 cm for various shield diameter combinations.

length of 60 cm for various combinations of shield diameters. For this simulation, we assumed 5-mm diameter gaskets with copper strips for all cases. One end of the optic is significantly thicker when using the same diameters for both shields. However, reducing the shield diameter on one side can increase the thickness to match the other end closely. The thickness uniformity is improved to 6.3% from 8.1% by changing one of the shields to 56 cm from 76 cm while maintaining the other at 76 cm. Thickness uniformity decreases when the shield diameters are reduced below the optimal value.

4 Experimental Validation of Simulation Results

We replicated several full-shell X-ray optics based on the inputs from the COMSOL simulations. Optimizing the shields and gasket dimensions consistently improved the shell thickness uniformity. The fabricated shell's thickness profiles agreed closely with the simulations over a wide range of thicknesses from 200 μm to 1.5 mm. As an example, we presented results for two shells with different dimensions and thicknesses. We replicated a shell from a small three-piece mandrel using large flat gaskets. The mandrel optical axial length is 6.1 cm. The maximum and minimum diameters are 4.6 and 4.52 cm, respectively. The mandrel has end caps of 3.9 cm on either side of the optic portion, making the total length of the mandrel 13.9 cm. For this three-piece mandrel design, we used flat gaskets with a 2-cm height above the mandrel surface. Figure 10 shows the mandrel setup with flat gaskets and shields just after plating. After releasing the mirror shell from the mandrel using a cold water bath, we measured the axial thickness using a GE CL5 ultrasonic thickness gauge. The nominal thickness of the optic is 1100 μm . The experimental thickness variation is $\sim 2.6\%$, which agrees closely with the 2.9% simulation result. Figure 11 compares the experimental measurement of the axial thickness profile with the COMSOL simulation results. The measured thickness variation of 2.6% is significantly lower than the previously replicated optics with non-optimized gaskets. The “as plated” measured shell thickness results are within 90% of the simulated COMSOL result values.

We also replicated a shell on a large single-piece mandrel to test the effect of shield optimization. The axial length of the optic is 60 cm. The mandrel has end caps of 5 cm on either side of the optic portion, making the total length of the mandrel 70 cm. This optic has maximum and minimum diameters of 7.6 and 6.2 cm, respectively. We used a small gasket with a copper strip to act as a cathode. The shield diameters of the top and bottom ends of the mandrel are 30 and 60 cm, respectively. Figure 12 shows the picture of the mandrel with the differential shield diameters and copper strip gaskets used for this experiment. Figure 13 shows the shell's simulated and measured axial thickness after separation. The nominal thickness of the optic is 500 μm . The thickness variation is 7.5% and matches closely with the simulation results. Copper cathodes on the gaskets helped to increase the thickness uniformity near the edges of the mirror shell. We fabricated several shells using a similar configuration, and the thickness distribution is identical in all cases.

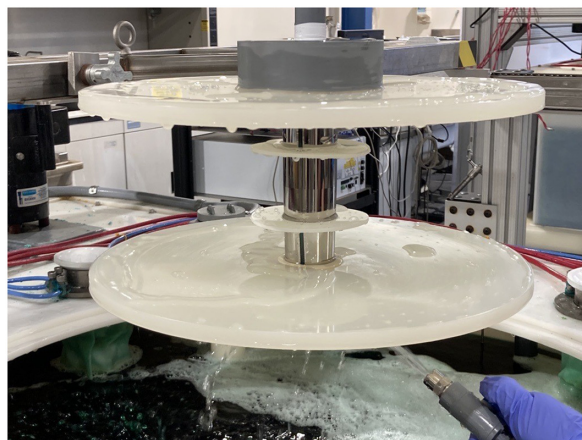


Fig. 10 Mandrel setup with flat gaskets and shields just after plating (picture credit: NASA).

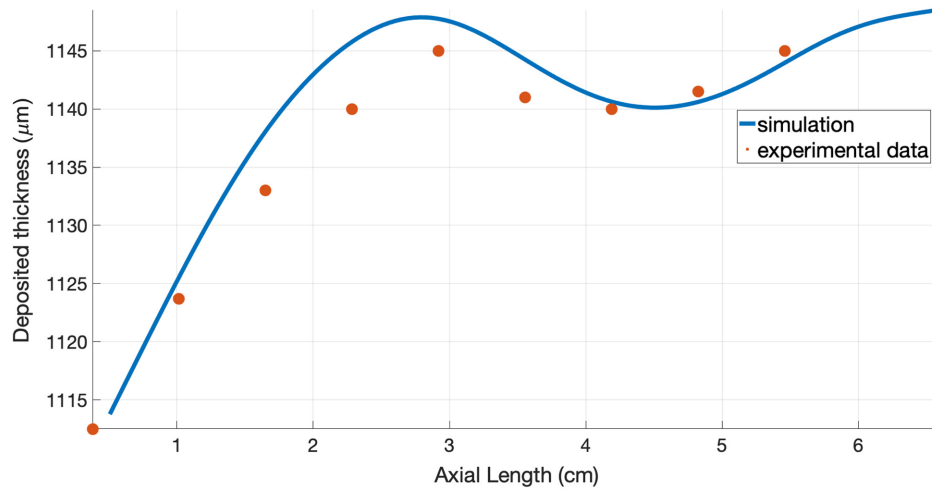


Fig. 11 Comparison of the measured axial thickness profile to results from the COMSOL simulation results of the configuration shown in Fig. 10. The thickness variation is under 3% and closely agrees with the simulations.



Fig. 12 Seventy-centimeter-long mandrel with differential shield diameters and copper strip gaskets (picture credit: NASA).

The residual thickness variation in our optics is due to the variation in the electric field distribution across the mandrel surface. Depending on the mandrel dimensions, gaskets and shields can only have a finite influence on the field distribution. As the axial length and slope of the optics increase, the gaskets and shields tend to have a lower influence on keeping the electric field uniform over the surface.

5 Effect of Electroforming Stress

Figure 1 shows that the applied anode current density influences the electroforming stresses. These stresses influence the figure of the replicated optic. Tensile stresses tend to make the electroformed optic stick to the mandrel, whereas the compressive stresses tend to release the optic fast and, sometimes, prematurely during the plating process. We plate at a tensile stress of 0.5 ksi for an optimal shell release process. For a flat circular substrate, the deposition stress results in the spherical curvature analytically given by Stoney's equation.²⁵ However, there is no analytical solution to estimate the nature and magnitude of the deformations of a complex shell geometry

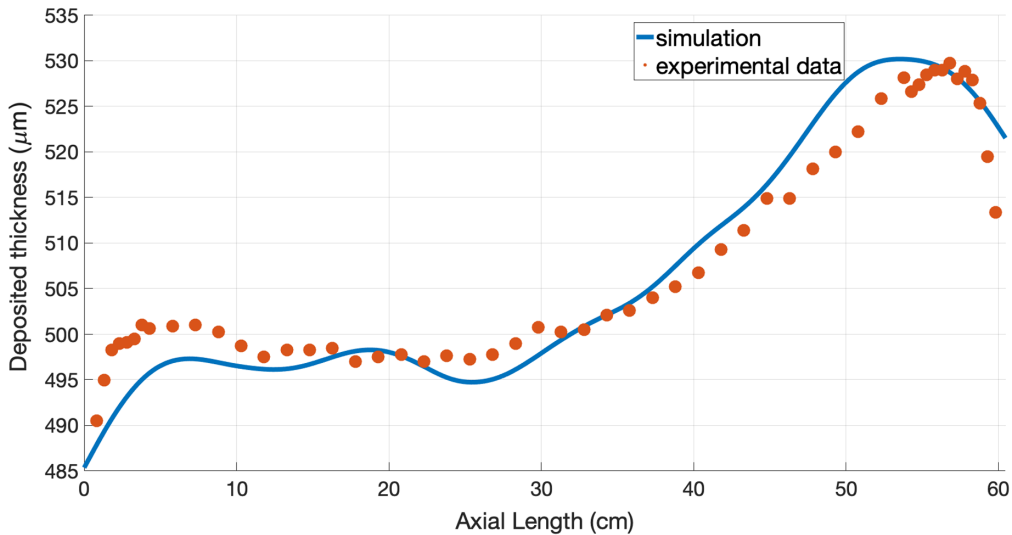


Fig. 13 Comparison of the measured axial thickness profile to the COMSOL simulation predictions for the configuration shown in Fig. 12 is plotted. The overall thickness variation is around 7.5%, as predicted, and closely agrees with the simulation.

such as full-shell Wolter I X-ray optics. Hence, we used FEM to estimate the effect of electroforming stress on full-shell optics. We observed that, unlike in the case of a flat circular optic, the stress-induced deformations are limited to the edges of the shell. Although the magnitude of the deformation changes as a function of the diameter and thickness of the shell, the deformation in every case is limited to near-edge regions.

We calculated the deformation due to electroforming stress using FEM built-in COMSOL Multiphysics. The model consists of the Wolter optic plated on a mandrel. Stress is applied by prescribing a temperature field to the plated shell. This method is analogous to applying thin film stresses to measure the deformation of a curved substrate, as presented by Chalifoux et al.²⁶ The deformation of full-shell optics due to coating stresses is discussed by Gurgew et al.²⁷ The applied temperature field acts similarly to the film stress deposited on a substrate as the applied temperature profile makes the optic locally expand or contract. The mandrel's thermal expansion coefficient in these simulations is set to zero to create the stress field in the plated optics with the applied temperature. By waiving the thermal expansion of the mandrel, the thermal expansion from the shell creates a stress field on the system. For these simulations, the shell is assumed to be in complete contact with the mandrel. In this configuration, the applied temperature directly translates to stress in the shell. Temperatures above the ambient temperature result in tensile stress, and the lower temperatures simulate compressive stresses. We tested this technique on a flat circular geometry to compare it with the established analytic results (Fig. 14). The

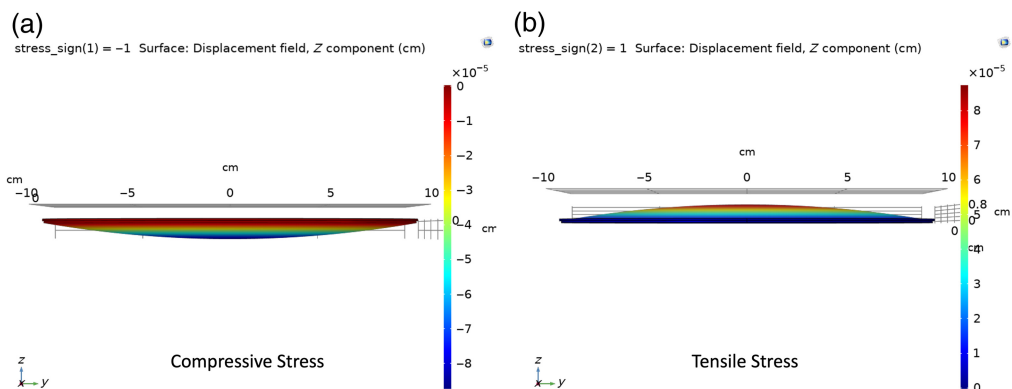


Fig. 14 FEM simulation of deposition stress on a flat circular substrate. Panel (a) shows the compressive stress, and panel (b) shows the tensile stress. In each case, the predicted stress results in curvature of the substrate, which agrees with our experimental studies.

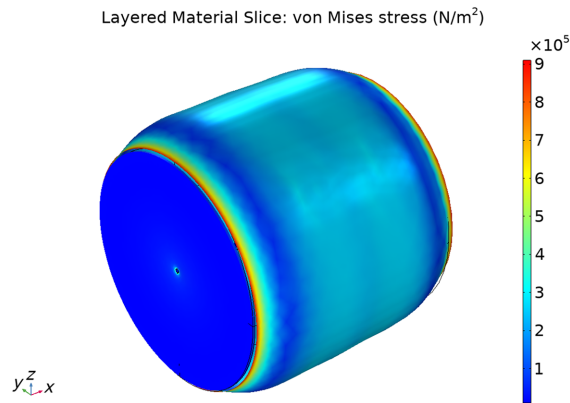


Fig. 15 FEM simulation of the effect of tensile deposition stress on a cylindrical shell. Most of the deformation is localized close to the edges of the shell.

deformation from the FEM is in the form of spherical curvature across the optic. The radius of curvature measures the stress, which closely matches the analytical solutions.

5.1 Figure Deformation in Full-Shell X-ray Optics

Plating stress-induced figure deformations are estimated using FEM modeling. Unlike in the case of flat substrates, deformation in full-shell X-ray optics is localized toward the edges of the shell. Tensile stress makes the shell ends flare in toward the mandrel (Fig. 15), and compressive stress makes the shell flare out. The direction and amount of flaring at the shell ends are proportional to the magnitude of the plating stress. Figure 16 shows the axial deformation of the shell for various plating stress values. For this simulation, we considered a 50-cm diameter shell with an axial length of 60 cm. The deformation errors correspond to an optic that is 1-mm thick. The magnitude of the edge deformation varies linearly with the stress. The flaring direction changes when the stress changes from positive tensile to negative compressive. The deformation near the center of the optic is due to the change in the slope of the optic at the intersection of parabolic and hyperbolic surfaces.

5.2 Experimental Validation of Stress Deformation

The axial profile of the mandrel was measured to determine the effect of stress on the axial deformation of the optics. Then, we compared the deformations with the axial shape of the shell. All axial measurements were taken using MSFC's vertical long trace profiler (VLTP). Axial errors on the mandrel are primarily due to residual errors from the polishing, whereas errors

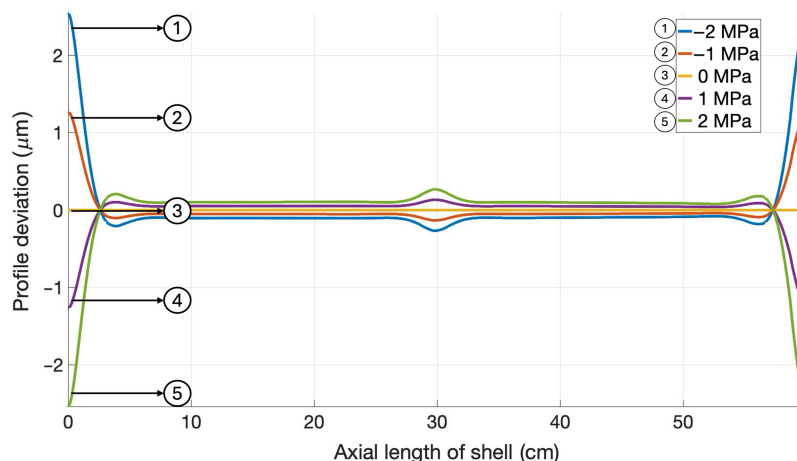


Fig. 16 Axial deformation of the shell for various plating stress values. The direction of edge flaring changes as stress moves from compressive to tensile. For this simulation, we considered a 50-cm-diameter shell with an axial length of 60 cm and 1-mm shell thickness.

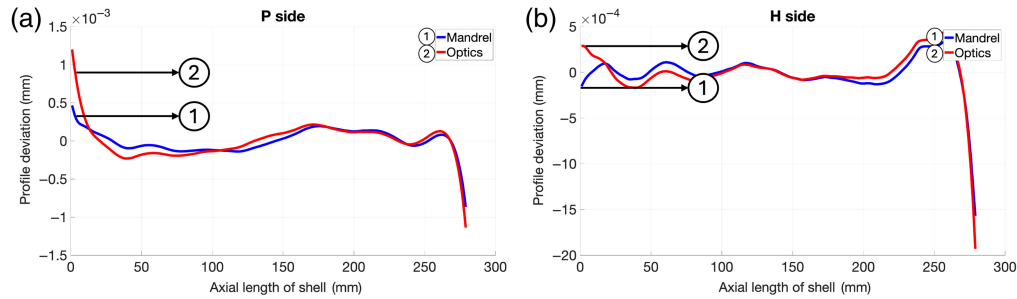


Fig. 17 VLTP measured axial scans of the mandrel and the optics. Measurements are taken on the outside of the mandrel and inside of the shell. Panels (a) and (b) show the comparison of the shell's parabolic and hyperbolic profiles to that of the mandrel. The electroforming process accurately replicates mid-spatial frequencies.

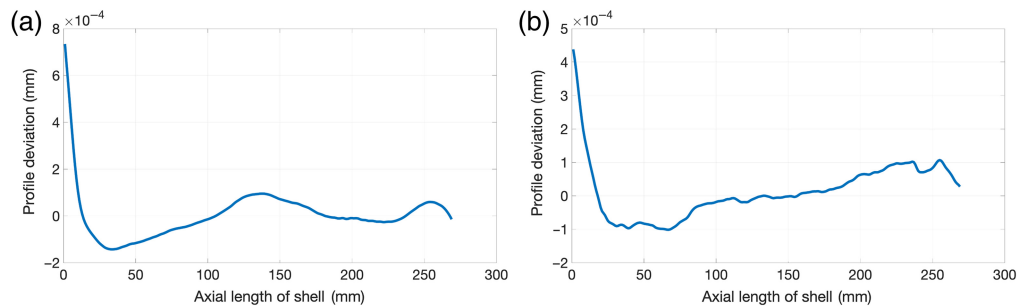


Fig. 18 Axial profile errors due to electroforming stress on (a) parabolic and (b) hyperbolic segments of the optic. Errors are predominantly focused on the edges of the shell.

on the optic include errors from the mandrel and additional errors due to the electroforming process. Figure 17 shows the axial error profile of the parabolic and hyperbolic sides of the mandrel and a single optics shell. The data clearly show that the electroforming process accurately replicates the mid-spatial frequencies from the mandrel. Both measurements are taken from the ends at the origin toward the intersection of the parabolic and hyperbolic sections. The measurements are taken on the outside of the mandrel and the inside of the shell for accurate comparison. The axial length of the optics is 29.1 cm, and the diameter of the optics is 13.9 cm at its center.

The difference between the axial profile errors of the mandrel and the shell gives the error contributed by the electroforming process (Fig. 18). One can observe that the replication errors are minimal at the center of the optic and significantly increase at the ends. We observed a similar effect for several other replicated optics. This effect correlates well with the impact of plating stress, as shown in Figs. 15 and 16. Replicated X-ray mirrors for the XMM-Newton telescope also reported trumpet-shaped deformation due to stress.²⁰ Hence, the deformation due to plating stress is the major contributor to the axial profile error. However, in a full-shell configuration, this effect has a minimal contribution to the overall performance of the optic as the deformation is localized to the edges.

5.3 Stress Deformation as a Function of Shell Thickness

In general, the stress-induced deformation is reduced as the thickness of the electroformed shell is increased because the stiffness strength of the optics increases with the thickness. Figure 19 shows the simulated axial deformation due to 1 MPa stress for a 50-cm diameter optics and 60-cm axial length. Even though the magnitude of the deformation is reduced, the deformation propagates deeper into the axial length for thicker-shell optics. The profile errors are localized to smaller areas for thin shells. The deformation is distributed to relatively larger areas as the shell's stiffness increases with thickness.

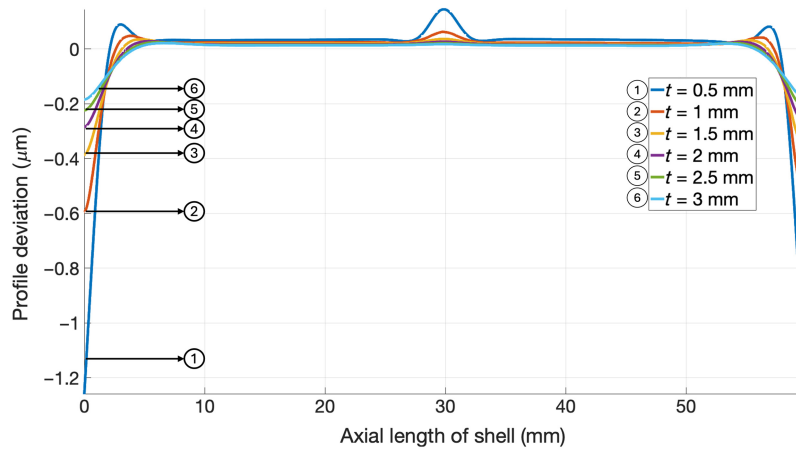


Fig. 19 Axial deformation due to 1-MPa stress for 50-cm-diameter optics and 60-cm axial length as a function of shell thickness. The flaring effect at the edge of the shell decreases as a function of shell thickness.

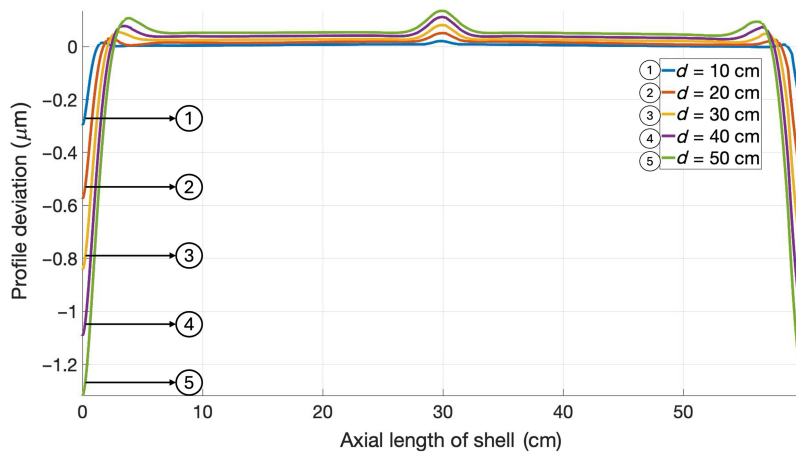


Fig. 20 Stress-induced axial profile errors for a 1-mm-thick optic at 1-MPa plating stress as a function of shell diameter. Larger-diameter shells experience larger flarings at the edge of the optics shell.

5.4 Effect of Optics Diameter

For a given shell thickness, the mechanical stiffness decreases with the increase in shell diameter. Hence, larger-diameter optics tend to have more notable deformation for a given plating stress. Figure 20 shows the stress-induced axial profile errors for a 1-mm-thick optic at 1 MPa plating stress for various shell diameters. The profile error gets larger and propagates deeper with the increase in the diameter of the optics. To counter this effect, one can proportionally increase the thickness of the shells with an increase in the diameter. However, as the error is localized close to the shell edge, its contributions toward the optical quality of the shell remain minimal.

5.5 Axial and Azimuthal Stress Variation

The deposition stress is directly proportional to the local electric field. Because the local electric field varies significantly with the mandrel geometry and the plating bath configuration, the plating stresses will not be uniform along the shell. Axial stress uniformity is controlled using optimized stress gaskets and shields in a similar fashion as described in Sec. 3. In the simulation framework, we studied the strain due to axially varying stress profiles for different cases. Interestingly, the axial deformation of the shell remained the same for various assumed axially varying stresses. The deformation profile correlated with the average stress value across the length but not with the shape of the stress profile. Hence, the overall stress value is more crucial

to maintaining the optics figure than the axial stress variation. In Sec. 3, we observed that the mandrel experiences elevated current densities near the edges when small gaskets without copper strips are used. This will increase the integrated stress value across the axial length. Hence, we can improve the optics figure by regulating the deposition stresses using optimized gaskets and shields. We observed significant improvements in the overall optics figure with optimized gaskets for smaller axial lengths than large ones. This is because the integrated stress value for small optics depends more on the edge stress variations than the large optics. For example, a 1-MPa stress on a 0.5-mm-thick 50-mm-diameter optics contributes to $\sim 0.5''$ HPD for a 600-mm axial length optics and $0.9''$ for a 100-mm axial length optics of the same thickness. However, our simulations showed that adding $\sim 10\%$ axial variation to the stress did not significantly change the performance of 600-mm-long optics, but for 100-mm-long optics, performance degraded to $3''$ HPD. We previously experimentally observed an improved imaging performance for small optics (axial lengths of 10 cm) using optimized gaskets.¹⁷ We found no noticeable effect for larger optics in varying gasket sizes (axial length of 60 cm).¹⁵

The plating bath is designed to have azimuthal uniformity in electric fields and deposition rates. Anodes are placed uniformly around the mandrel. The mandrel spins around its axis during plating to improve the azimuthal uniformity further. From both modeling studies and experimental results, we observed that azimuthal thickness variance is negligible. Hence, the stress variation in the azimuthal axis is not a significant source of errors in optics fabrication. However, we assumed significant azimuthal stress variations for completeness and studied its effect on the optics figure. Even with substantial variations (over 100%) in the azimuthal stress, there is no significant variation in the circularity errors in the shell, indicating that the plating stress is not a substantial contributor to the non-circularity of the shell.

6 Discussion and Summary

The critical scientific requirements of an X-ray flagship mission drive the X-ray optics development at MSFC. Our primary objectives include achieving sub-arcsecond angular resolution and a substantial effective area. To accomplish this, we employ an electroforming replication process that allows a full-shell configuration and fabricating thin shells. This allows us to replicate optics with large effective areas.

Our in-house developed optic for IXPE previously demonstrated the feasibility of this approach by achieving an impressive effective area-to-weight/volume ratio.²⁸ However, despite our success, the angular resolution achievable with current technology remains significantly larger than proposed for the Lynx concept study. Our focus lies in systematically understanding and enhancing every step of the fabrication process to elevate the imaging quality.

This paper delved into two critical factors: thickness uniformity and electroforming stress. These aspects contribute to imaging errors of less than 2 arcsec. Such deviations are negligible for optics with a 15-arcsec threshold (as seen in XMM-Newton) and become dominant when aiming for sub-5 arcsec optics.

Simulations to study the electric field distribution inside the plating tank prove advantageous in regulating electroformed mirror-shell thickness uniformity. Optimizing gaskets and shield dimensions consistently produces optics with uniform thickness. Large GHs and copper strips are used to reduce the edge non-uniformity of the mirror shell, and differential gasket and shield dimensions help regulate the thickness uniformity across the entire axial length of the shell. The thickness distribution in the azimuthal direction is generally uniform due to the rotational symmetry of the electroforming tank configuration and mandrel rotation during plating. Using this simulation-led technique, we repeatedly produce full-shell X-ray optics with under 5% axial thickness variation. Using FEM, we estimated the effect of deposition stress on the axial figure errors of the replicated optics. The stress-induced error predominantly affects the ends of the shell, which has been observed experimentally. We also estimated the plating stress effects on a shell as a function of thickness and diameter. Deposition stresses have a minimal effect on the optical performance of the optics as the errors are confined to the edges of the shell. This is one of the major advantages of the full-shell optics geometry. Gasket optimization improves shell separation from the mandrel and figure because the deposition stress is directly proportional to the local current density. The optimization process is more critical for optics with

large graze angles. We routinely custom-design a unique set of gaskets and shields for each mandrel geometry. In some cases, with small axial length mirrors, using custom gaskets also improved the imaging performance of the optics. This improvement could be due to reduced overall stress on the shell as edge fields are regulated. However, we need further investigations to understand this relationship. We are investigating the effect of thickness uniformity on the shell release mechanism and non-circularity of the shell.

Code and Data Availability

The authors confirm that the data supporting the findings are fully available in the article. Raw data for this study are available from the corresponding author upon request.

Acknowledgments

The primary source of funding for this work is through the NASA Astrophysics Division Internal Scientist Funding Model (ISFM). The authors want to recognize the MSFC Optical Systems Design and Fabrication Branch (ES23) for supporting the X-ray Optics ISFM tasks.

References

1. B. D. Ramsey et al., "Development of hard X-ray optics at MSFC," *Proc. SPIE* **4851**, 631–638 (2003).
2. B. Ramsey, "Replicated nickel optics for the hard-X-ray region," *Exp. Astron.* **20**, 85–92 (2005).
3. K. Kilaru et al., "Full-shell x-ray optics development at NASA Marshall Space Flight Center," *J. Astron. Telesc. Instrum. Syst.* **5**(2), 021010 (2019).
4. G. Boella et al., "BeppoSAX, the wide band mission for X-ray astronomy," *Astron. Astrophys. Suppl. Ser.* **122**(2), 299–307 (1997).
5. F. Jansen et al., "XMM-Newton observatory*—I. the spacecraft and operations," *A&A* **365**(1), L1–L6 (2001).
6. D. N. Burrows et al., "The SWIFT X-ray telescope," *Space Sci. Rev.* **120**, 165–195 (2005).
7. P. Predehl et al., "The eROSITA X-ray telescope on SRG," *A&A* **647**, A1 (2021).
8. M. Pavlinsky et al., "The art-XC telescope on board the SRG observatory," *A&A* **650**, A42 (2021).
9. B. D. Ramsey et al., "The Imaging X-ray Polarimetry Explorer (IXPE): technical overview IV," *Proc. SPIE* **11821**, 118210M (2021).
10. B. D. Ramsey et al., "HERO: high-energy replicated optics for a hard-X-ray balloon payload," *Proc. SPIE* **4138**, 147–153 (2000).
11. J. Gaskin et al., "High energy replicated optics to explore the sun: hard X-ray balloon-borne telescope," in *IEEE Aerosp. Conf.*, pp. 1–11 (2013).
12. S. Krucker et al., "First images from the focusing optics X-ray solar imager," *Astrophys. J. Lett.* **793**, L32 (2014).
13. S. D. Christe et al., "Foxsi-2: upgrades of the focusing optics X-ray solar imager for its second flight," *J. Astron. Instrument.* **5**(1), 1640005 (2016).
14. S. Musset et al., "Ghost-ray reduction and early results from the third FOXSI sounding rocket flight," *Proc. SPIE* **11118**, 1111812 (2019).
15. W. H. Baumgartner et al., "High resolution full shell replicated X-ray optics for FOXSI-4," *Proc. SPIE* **12679**, 126790C (2023).
16. M. Pavlinsky et al., "ART-XC/SRG overview," *Proc. SPIE* **10699**, 106991Y (2018).
17. P. R. Champey et al., "Toward the fabrication of a 5 micron-resolution Wolter microscope for the National Ignition Facility (invited)," *Rev. Sci. Instrum.* **93**, 113504 (2022).
18. M. C. Weisskopf et al., *Chandra X-ray Observatory*, SPIE Press, Bellingham, Washington (2000).
19. J. A. Gaskin et al., "Lynx mission concept status," *Proc. SPIE* **10397**, 103970S (2017).
20. D. de Chambure et al., "Lessons learned from the development of the XMM optics," *Proc. SPIE* **3737**, 2–17 (1999).
21. A. Ito et al., "Electrodeposition simulation for fabricating Wolter mirrors of X-ray telescopes," *Proc. SPIE* **11837**, 118370D (2021).
22. P. Singam et al., "Optimizing the electroforming process to enhance the thickness uniformity of full shell X-ray optics," *Proc. SPIE* **12679**, 126790B (2023).
23. D. Engelhaupt, B. Ramsey, and C. Speegle, "Electrodeposition of low stress nickel-phosphorus alloys for precision component fabrication," *Proc. SPIE* (2000).
24. C. Multiphysics, *Introduction to COMSOL Multiphysics®*, p. 2018, COMSOL Multiphysics, Burlington, MA (1998).

25. G. Stoney, “The tension of metallic films deposited by electrolysis,” *Proc. R. Soc. Lond. Ser. A* **82**(553), 172–175 (1909).
26. B. D. Chalifoux et al., “Simulations of film stress effects on mirror segments for the Lynx X-ray observatory concept,” *J. Astron. Telesc. Instrum. Syst.* **5**, 021004 (2019).
27. D. N. Gurgew and S. P. Singam, “Characterization of NiC multilayer coating stress for X-ray optic applications,” *Proc. SPIE* **12679**, 126790N (2023).
28. B. D. Ramsey et al., “Optics for the Imaging X-ray Polarimetry Explorer,” *J. Astron. Telesc. Instrum. Syst.* **8**(2), 024003 (2022).

Biographies of the authors are not available.